Letter

Topological Hall effect in the antiferromagnetic Dirac semimetal EuAgAs

Antu Laha,[1,*] Ratnadwip Singha,[2,†] Sougata Mardanya,[1] Bahadur Singh,[3,‡] Amit Agarwal,[1] Prabhat Mandal,[2] and Z. Hossain[1,§]

[1]*Department of Physics, Indian Institute of Technology, Kanpur 208016, India*

[2]*Saha Institute of Nuclear Physics, HBNI, 1/AF Bidhannagar, Calcutta 700 064, India*

[3]*Department of Condensed Matter Physics and Materials Science, Tata Institute of Fundamental Research, Mumbai 400005, India*

(Received 30 June 2020; revised 8 December 2020; accepted 1 June 2021; published 21 June 2021)

The nontrivial magnetic texture in real space gives rise to the intriguing phenomenon of the topological Hall effect (THE), which is relatively less explored in topological semimetals. Here, we report a large THE in the antiferromagnetic (AFM) state in single crystals of EuAgAs, an AFM Dirac semimetal. EuAgAs hosts an AFM ground state below $T_N = 12$ K with a weak ferromagnetic component. The in-plane isothermal magnetization below T_N exhibits a weak metamagnetic transition. We also observe chiral anomaly induced positive longitudinal magnetoconductivity, which indicates a Weyl fermion state under an applied magnetic field. The first-principles calculations reveal that EuAgAs is an AFM Dirac semimetal with a pair of Dirac cones, and therefore a Weyl semimetallic state can be realized under time-reversal symmetry breaking via an applied magnetic field. Our study establishes that EuAgAs is a system for exploiting the interplay of band topology and the topology of the magnetic texture.

DOI: 10.1103/PhysRevB.103.L241112

The rich interplay between the electronic structure and topology in materials ensures a variety of topological states. These include topological states as diverse as Dirac or Weyl semimetals (DSMs or WSMs), topological insulators, topological magnets, and topological superconductors [1–17]. The topological states of matter are robust and cannot be destroyed by local disorder and perturbations. Among these, the topological magnets are particularly appealing since they support tunable phases and electromagnetic responses which are exciting for fundamental science as well as for next-generation technological applications. Notable examples are magnetic WSMs, where magnetization can enhance the net Berry flux through Weyl node tuning and, as a consequence, the anomalous Hall effect (AHE) is enhanced [11,12,18,19]. Despite their recent experimental realization, the current choice of available materials is quite limited. Therefore the search for new topological magnets with novel electromagnetic responses is of immense importance.

Furthermore, topologically nontrivial spin textures in magnetic systems give rise to another type of Hall effect, termed the topological Hall effect (THE). Such nontrivial spin textures in real space are generated either by geometrical frustration or by antisymmetric Dzyaloshinskii-Moriya (DM) interaction [20]. When an electron moves through these spin textures, it acquires a real-space Berry phase, which acts as an effective magnetic field. This effective magnetic field is proportional to the scalar spin chirality of the magnetic structure and leads to the THE [21]. The nontrivial spin textures can be described by a finite topological number $Q = (1/4\pi)\int \hat{n} \cdot (\partial\hat{n}/\partial x \times \partial\hat{n}/\partial y)\, dxdy$, where $\hat{n}$ is the unit vector in the direction of local magnetization. An integer value of Q, with $|Q| \geqslant 1$, results in the THE [22–26]. Recent studies have shown that achiral polar crystals with C_{nv} symmetry allow DM interaction which can stabilize the Neel-type skyrmion phase with a large THE [27–29]. While the THE has been observed in various families of materials as diverse as B20 compounds, antiferromagnets, pyrochlore lattices, and correlated oxide thin films [22,23,30–38], it remains largely unexplored in topological WSMs with a few exceptions such as CeAlGe [27].

In this Research Letter, we report a large THE in single-crystalline EuAgAs, an antiferromagnetic (AFM) DSM. EuAgAs crystallizes in a hexagonal symmetry with $P6_3/mmc$ (D_{6h}) space group. This symmetry group can generate finite scalar magnetization chirality as well as skyrmion or biskyrmion phases in magnetic materials, suitable for realizing the THE [25,26]. We explore the interplay between the topology and magnetism in EuAgAs below $T_N = 12$ K. We also observe chiral anomaly induced positive longitudinal magnetoconductivity associated with the Weyl fermion state under an applied magnetic field. From the first-principles calculations, we conclude that EuAgAs realizes an AFM DSM state with a pair of Dirac cones lying on the C_{3z} axis. Thus our study establishes EuAgAs as an AFM DSM with anomalous transport properties.

EuAgAs single crystals were grown by the flux method with bismuth as an external flux [39]. Magnetotransport, magnetization, and specific heat measurements were carried out in a physical property measurement system and superconducting quantum interference device vibrating-sample magnometer

*antuiitk2012@gmail.com

†Present address: Department of Chemistry, Princeton University, Princeton, New Jersey 08544, USA.

‡bahadur.singh@tifr.res.in

§zakir@iitk.ac.in

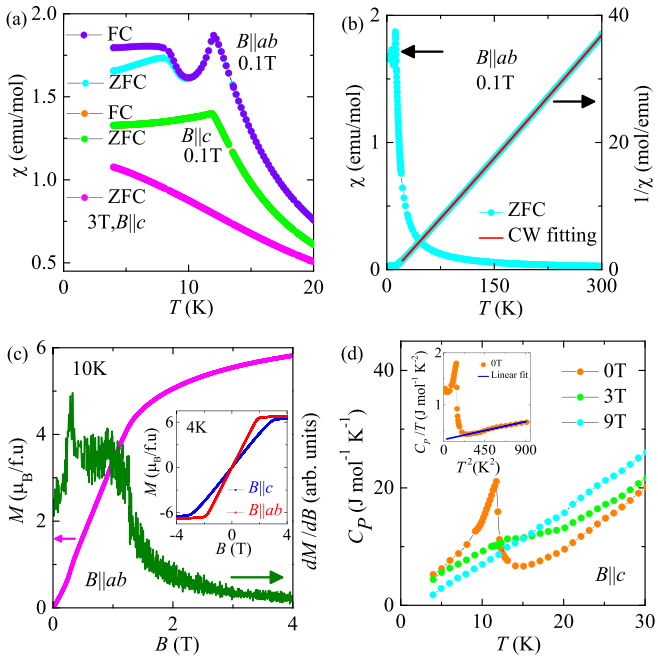

FIG. 1. (a) Temperature-dependent magnetic susceptibility in zero-field-cooled (ZFC) and field-cooled (FC) conditions for $B \parallel c$ and $B \parallel ab$. (b) The ZFC magnetic susceptibility (cyan markers) and the Curie-Weiss (CW) fitting (solid red line) to the $1/\chi$ curve in the temperature range 20–300 K for $B \parallel ab$. (c) Isothermal magnetization (M) and the first derivative of M (dM/dB) at 10 K for $B \parallel ab$. The inset shows M vs B at 4 K for $B \parallel c$ and $B \parallel ab$. (d) Temperature dependence of the specific heat at various magnetic field values up to 9 T. The solid blue line in the inset fits the formula $C_P/T = \gamma + \beta T^2$.

(SQUID VSM, Quantum Design). The experimental and computational details are given in the Supplemental Material (SM) [40–49]. To resolve the magnetic ordering in EuAgAs, we have measured the temperature-dependent zero-field-cooled (ZFC) and field-cooled (FC) susceptibility (χ) along the crystallographic c axis ($B \parallel c$) and ab plane ($B \parallel ab$) as shown in Fig. 1(a). χ exhibits a peak at 12 K due to AFM ordering of the Eu^{2+} moments which is suppressed by the application of a magnetic field of 3 T. It is evident from Fig. 1 that the nature of the $\chi(T)$ curve for $B \parallel ab$ is quite different from a typical AFM system [50]. $\chi(T)$ shows nonmonotonic T dependence below T_N. After a sharp drop below T_N, $\chi(T)$ starts to increase and saturates below 8 K. A small bifurcation between ZFC and FC curves is also observed below 8 K. This behavior of χ suggests the presence of a weak ferromagnetic (FM) component and competition between AFM and FM interactions [51]. Above 20 K, we have fitted the $1/\chi$ for $B \parallel ab$ with the modified Curie-Weiss law, $\chi(T) = \chi_0 + C/(T - \theta_p)$ [Fig. 1(b)]. Here, χ_0, C, and θ_P are the temperature-independent susceptibility, Curie constant, and Curie-Weiss temperature, respectively. The estimated effective magnetic moment of Eu^{2+} is 8.03 μ_B for $B \parallel ab$ and 7.68 μ_B for $B \parallel c$, which are close to the theoretical value of $g\sqrt{S(S+1)}\mu_B = 7.94$ μ_B for $S = 7/2$. The fit yields $\theta_P \approx$ 10.4 K and 8.7 K for $B \parallel ab$ and $B \parallel c$, respectively [see the Supplemental Material (SM)] [40].

To obtain further insight into the magnetic ground state, we have measured isothermal magnetization $M(B)$ for both orientation $B \parallel ab$ and orientation $B \parallel c$. For $T < T_N$, M increases faster with an increase in B and saturationlike behavior appears at a lower field for $B \parallel ab$ (∼2 T) compared with $B \parallel c$ (∼3 T) [see the inset of Fig. 1(c)]. The $M(B)$ curve at 10 K shows a weak anomaly below 1 T for $B \parallel ab$ as shown in Fig. 1(c). To analyze this behavior, we plot dM/dB as a function of B, in which a peak is observed around ∼0.3 T. At low temperature, the $M(B)$ curve for $B \parallel ab$ exhibits an upward curvature and a weak hysteresis at low field (see the SM for details) [40]. These behaviors indicate a weak metamagnetic transition for $B \parallel ab$. However, no anomaly is observed for $B \parallel c$ at low field. It is also clear from Figs. 1(a) and 1(c) that the easy axis of magnetization is on the ab plane. The observed behavior is qualitatively similar to that reported for the isostructural EuCuAs compound [52]. Both the value and T dependence of χ below T_N in EuCuAs are also sensitive to the direction of the applied magnetic field, and θ_P is positive. To reconcile the observed behavior of magnetic properties, A-type AFM ordering was proposed for EuCuAs where Eu^{2+} spins align ferromagnetically within the ab plane and antiferromagnetically between the planes. Our theoretical results discussed below also support such a spin state for EuAgAs. We have also measured the field dependence of magnetization at a high temperature above T_N as shown in the SM [40]. Even well above T_N, M is large and shows nonlinear B dependence (e.g., at 20 K).

The temperature dependence of specific heat C_P at various fields up to 9 T is shown in Fig. 1(d). $C_P(T)$ shows a sharp λ-like peak at $T_N = 12$ K which is suppressed with an increase in the magnetic field. The fit to the zero-field $C_P(T)$ curve in the range 16–30 K with the expression $C_P = \gamma T + \beta T^3$ yields $\gamma \sim 334$ mJ mol^{-1} K^{-2} [inset of Fig. 1(d)]. A large value of γ has also been reported for $EuFe_2P_2$ and $EuCr_2As_2$ and was attributed to magnon contributions from the ordering of Eu moments [53,54].

We now discuss the electrical resistivity ρ and magnetoresistance (MR) of EuAgAs. Figure 2(a) shows that ρ decreases almost linearly with decreasing T down to 40 K. With a further decrease in T below 40 K, ρ starts increasing due to the influence of magnetic ordering and reaches a maximum at $T_N = 12$ K. The transverse magnetoresistance (TMR) shows a cusplike feature at very low magnetic field which is attributed to the weak antilocalization [Fig. 2(b)]. The transition from the AFM state to a spin-polarized state is marked by a sharp maximum around 3 T. In the spin-polarized state, the TMR becomes negative and saturates at high fields. The TMR is negative up to 20 K. However, the TMR becomes positive well above T_N ($T > 20$ K). In contrast, the longitudinal magnetoresistance (LMR) is negative both below and above T_N and increases monotonically with the field, as shown in Fig. 2(c). The negative LMR increases continuously with a decrease in T from 2.7% at 100 K to 66% at 4 K. The negative MR at low temperature may partly arise due to the suppression of spin-disorder scattering as in the case of several Eu-based compounds where MR can be scaled with magnetization as discussed in the SM [40,55,56]. However, the negative LMR in the paramagnetic region well above T_N is surprising. Also, the significantly larger value of the LMR and the nature of

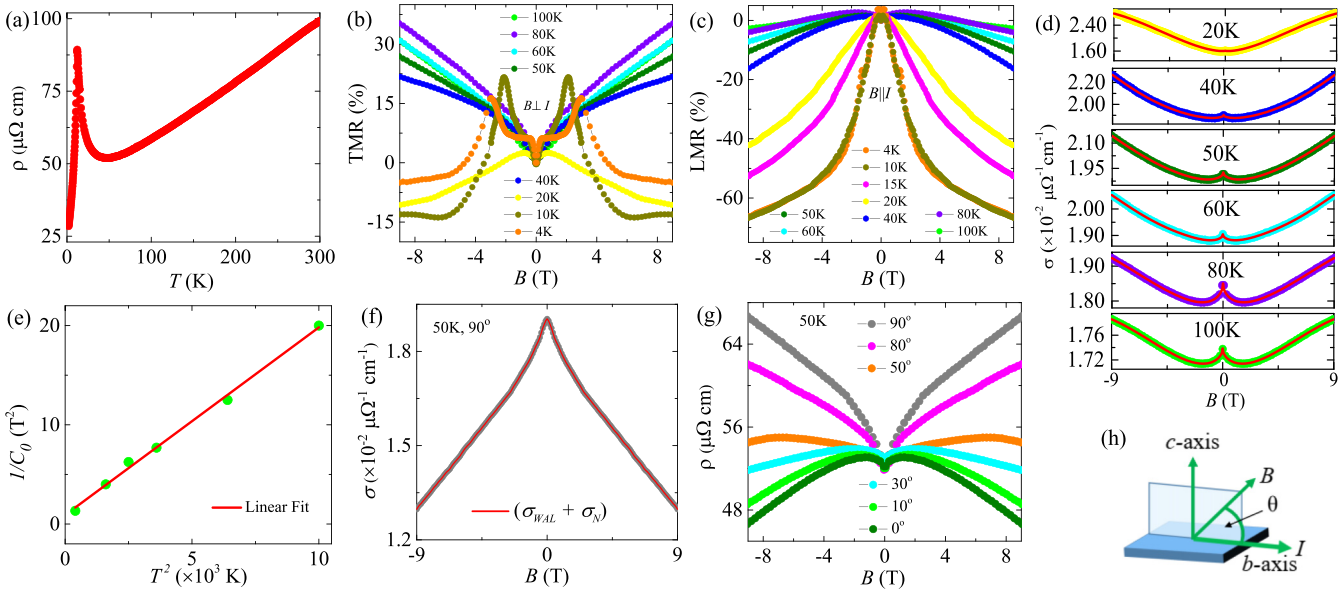

FIG. 2. (a) Temperature-dependent resistivity at zero magnetic field. (b) Transverse magnetoresistance ($B \perp I$) as a function of B at different temperatures up to 100 K. (c) Longitudinal magnetoresistance ($B \parallel I$) as a function of B at various temperatures. (d) The magnetic field dependence of longitudinal conductivity ($\sigma = 1/\rho$) at various T ($\theta = 0°$). The solid red lines show the fit to Eq. (1), which includes antilocalization and chiral anomaly induced corrections to conductivity. (e) $1/C_0$ vs T^2; the red solid line indicates a linear fitting. (f) Transverse conductivity [$\sigma = \rho/(\rho^2 + \rho_{yx}^2)$] for 50 K ($\theta = 90°$) fits to the expression $\sigma(B) = \sigma_{\mathrm{WAL}} + \sigma_N = (\sigma_0 + a\sqrt{|B|}) + (\rho_0 + AB^2)^{-1}$. (g) Resistivity as a function of B at various angles θ at 50 K. (h) Schematic diagram of the experimental setup.

its field dependence suggest that LMR at low temperature is dominated by a nonmagnetic component. Regarding the physical mechanism behind the observation of the negative LMR, the possibility of the current jetting effect can be ruled out as discussed in the SM [40,57]. We attribute the negative LMR to the chiral anomaly associated with the presence of opposite chirality Weyl fermions. This is supported by the successful fitting of the magnetoconductivity (MC) data to the semiclassical formula [Fig. 2(d)] [58],

$$\sigma(B) = \sigma_{\mathrm{WAL}}\,(1 + C_0 B^2) + \sigma_N. \tag{1}$$

Here, $\sigma_{\mathrm{WAL}} = (\sigma_0 + a\sqrt{|B|})$ is the conductivity due to the weak antilocalization effect, and $\sigma_N = (\rho_0 + AB^2)^{-1}$ represents the normal conductivity originating from the conventional Fermi surface (other than Weyl points). ρ_0 denotes the zero-field resistivity, and a and A are two constants. The positive MC (or negative MR) depends on $C_0 B^2$, where the positive value of C_0 originates from the finite $\mathbf{E} \cdot \mathbf{B}$ term which produces chiral charge current in the WSM [59–61]. Remarkably, we observe a chiral anomaly and weak antilocalization up to relatively high temperature [Fig. 2(d)] as in the case of YbPtBi [62]. Notably, we do not find any B-linear resistivity terms in our fitting, which indicates that there are no electron pockets in the quantum limit [63]. The temperature dependence of C_0 can be described by the relation $C_0 \propto v_F^3 \tau_v/(T^2 + \mu^2/\pi^2)$, where v_F, τ_v, and μ are the Fermi velocity, chirality-changing scattering time, and chemical potential, respectively [64]. The linear fitting to the curve $1/C_0$ vs T^2 as shown in Fig. 2(e) further supports the presence of a chiral anomaly in the temperature range 20–100 K. The estimated value of τ_v is 2.8×10^{-12} s. A similar range of scattering timescales has also been seen in other Weyl semimetals [62,65,66]. The chiral anomaly induces positive MC only for the longitudinal case when $I \parallel B$, and this is not present in the transverse case ($\mathbf{E} \cdot \mathbf{B} = 0$). Notably, the transverse MC can be expressed as $\sigma^T(B) = (\sigma_0 + a\sqrt{|B|}) + (\rho_0 + AB^2)^{-1}$, without a chiral anomaly. The successful fitting of MC data at 50 K to this expression further confirms that the origins of LMR and TMR are quite different and the cusplike feature is due to the weak antilocalization [Fig. 2(f)]. We have further fitted the MC data with the Hikami-Larkin-Nagaoka formula to establish the weak antilocalization effect up to 100 K and shown the variation of the phase coherence length with temperature in the SM [40,67–69].

Figure 2(g) shows the magnetic-field-dependent resistivity at various angles θ between B and I for 50 K [the directions of B and I are schematically shown in Fig. 2(h)]. The MR shows a maximum negative value at $\theta = 0°$ ($= -10\%$) and decreases with increasing θ. The MR becomes positive for $\theta > 30°$ and reaches maximum at $\theta = 90°$ (=29%). Similar angle-dependent behavior of the MR has also been reported in other WSMs [62,70]. We have also measured the directional dependence of the MR by fixing the angle between B and I and observed a twofold symmetric anisotropy pattern at 4 K (details in the SM) [40].

The experimental Hall resistivity after removing the MR contribution using the expression $\rho_{yx} = [\rho_{yx}(B) - \rho_{yx}(-B)]$ is shown in Fig. 3(a). The negative and linear ρ_{yx} for 20 K $\leqslant T \leqslant$ 300 K indicates that electrons are the majority carriers. We estimate the carrier density n and Hall mobility μ using the relations $n = 1/(eR_0)$ and $\mu = R_0/\rho_{(B=0)}$, where R_0 is the slope of the $\rho_{yx}(B)$ curve. The temperature dependence of n

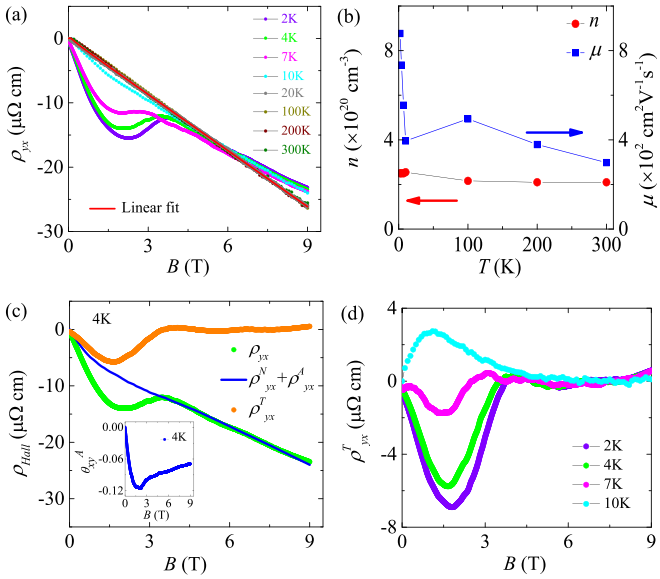

FIG. 3. (a) The Hall resistivity ρ_{yx} as a function of B ($B \parallel c$) at various temperatures. (b) Charge carrier density n and mobility μ vs temperature. (c) Hall resistivity (green markers) fitted to the conventional Hall contribution $\rho_{yx} = \rho^N_{yx} + \rho^A_{yx}$ at 4 K (blue solid line). The clear deviation from the conventional Hall resistivity indicates the presence of an additional term: the topological Hall resistivity (orange markers). The inset shows the anomalous Hall angle as a function of B at 4 K. (d) Topological Hall resistivity at various temperatures.

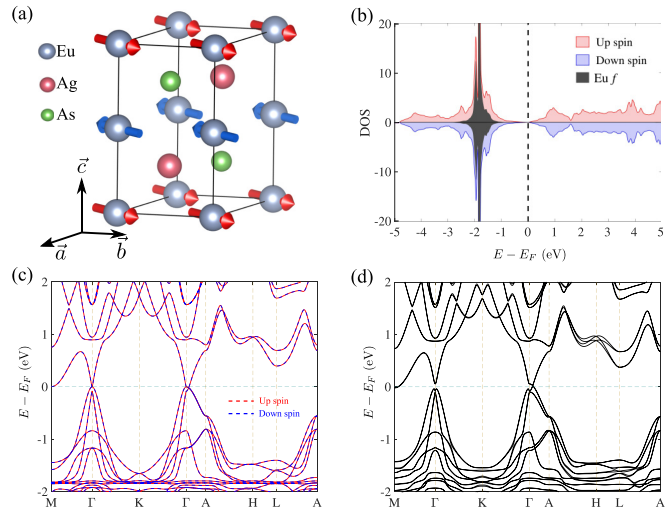

FIG. 4. (a) Orientation of Eu spins in the antiferromagnetic EuAgAs. (b) The density of states (DOS). The partial DOS of spin-up and spin-down states is shown in red and blue, respectively. The DOS associated with the localized Eu f states is shown in gray. (c) Band structure along the high-symmetry directions without spin-orbit coupling (SOC). The red and blue identify spin-up and spin-down states. (d) Band structure with SOC with spins along the *ab* plane. The Dirac band crossings are seen along the Γ-*A* direction.

and μ is shown in Fig. 3(b). We find that the carrier density is of the order of 10^{20} cm^{-3}, which remains almost temperature independent.

The Hall resistivities for $T \leqslant 10$ K show an anomaly below 3 T, which is quite prominent at low temperature. This behavior may be reminiscent of the anomalous Hall effect (AHE) observed in AFM Weyl semimetals. The AHE is empirically modeled as $\rho^A_{yx} = S_0\rho^2 M$, S_0 being a field-independent parameter. However, we find that below 3 T, the observed ρ_{yx} deviates from the fitting of the empirical Hall resistivity $\rho_{yx} = \rho^N_{yx} + \rho^A_{yx}$, as shown in Fig. 3(c). We also tried fitting ρ_{yx} with the conventional two-carrier model, but it fails to reproduce the anomaly (details in the SM) [40]. This clearly suggests the presence of an extra contribution to the Hall resistivity, which we attribute to the topological Hall effect [23,27].

By combining both the AHE and the THE in the AFM state, the total Hall resistivity can be expressed as [23]

$$\rho_{yx} = \rho^N_{yx} + \rho^A_{yx} + \rho^T_{yx} = R_0 B + S_0\rho^2 M + \rho^T_{yx}. \qquad (2)$$

Here, ρ^T_{yx} denotes the topological Hall resistivity arising from the chiral magnetization texture. Since ρ^T_{yx} vanishes in the fully spin-polarized state due to the absence of spin chirality, we execute a linear fit to the curve ρ_{yx}/B vs $\rho^2 M/B$ in the field range $4\ \text{T} \leqslant B \leqslant 9$ T. From the fitting, we estimate $R_0 = -2.51\ \mu\Omega$ cm T^{-1} and $S_0 = -1.72 \times 10^{-3}\ (\mu\Omega\,\text{cm})^{-1}\,\mu_B^{-1}$. Using these parameters, ρ^T_{yx} can be obtained by subtracting $\rho^N_{yx} + \rho^A_{yx}$ from ρ_{yx}, which is shown in Fig. 3(c) [23,27,71]. We estimate the maximum amplitude of ρ^T_{yx} at 2 K to be approximately $-7\ \mu\Omega$ cm [Fig. 3(d)]. This value of ρ^T_{yx} is quite large. In order to compare the THE, we estimate the topological Hall angle, $\Theta^T_{xy} = \sigma^T_{xy}/\sigma$, where σ^T_{xy} and σ are the topological Hall conductivity and magnetoconductivity, respectively. The maximum amplitude of Θ^T_{xy} (∼0.17) is comparable to that obtained in the magnetic Weyl semimetals GdPtBi (∼0.17) and YbPtBi (∼0.18) [19,62]. We have also estimated the anomalous Hall angle ($\theta^A_{xy} = \sigma^A_{xy}/\sigma$) [inset of Fig. 3(c)]. The maximum amplitude of θ^A_{xy} is 0.11, which is compared with some other known AFM Weyl semimetals in Table I of the SM [13,19,40,72–74].

We delineate the AFM DSM state of EuAgAs in Fig. 4. The unit cell consists of six atoms, in which Eu atoms occupy the Wyckoff position 2a and form a hexagonal stacking along the z direction. The Ag and As atoms are placed at Wyckoff positions 2d and 2c, respectively, to form hexagonal layers which are sandwiched between the Eu layers, satisfying the overall inversion symmetry. To consider the possible magnetic configuration of EuAgAs, we investigated three AFM spin configurations (see the SM for details) [40]. The lowest energy is obtained for the in-plane AFM [110] configuration as shown in Fig. 4(a). This is consistent with our measured magnetic properties. The AFM ordering of the Eu 4f spins is further demonstrated in Fig. 4(b), where the density of states (DOS) in the valence band region is dominated by the Eu f states, which is equal but opposite for spin-up and spin-down states. Moreover, EuAgAs has a vanishingly small DOS at the Fermi level, which confirms its semimetallic electronic state. This is further showcased in the band structure without spin-orbit coupling (SOC) in Fig. 4(c). The valence and conduction bands derived for both the spin states are seen to cross along the Γ-*A* direction with an inverted band ordering at the Γ point. The band structure with SOC is shown in Fig. 4(d). We find that the EuAgAs crystals have an inversion symmetry I, along with an effective time-reversal symmetry

$S = \Theta\tau_{1/2}$, where Θ is the time-reversal operator and $\tau_{1/2}$ is the translation vector connecting spin-up and spin-down atoms. Owing to these two symmetries, each of the bands in AFM EuAgAs remains twofold spin degenerate. We find that while the nodal band crossings without SOC are lifted, there are two symmetry-related fourfold degenerate band crossing points along the Γ-A directions as shown in Fig. 4(d). EuAgAs thus realizes a robust AFM DSM ground state with a pair of Dirac cones in the vicinity of the Fermi energy, on the C_{3z} rotation axis.

We next turn to discuss the possible reason behind the AHE and THE observed in EuAgAs. To confirm whether the Dirac nodes in EuAgAs can split into a pair of Weyl nodes on applying a magnetic field, we calculated the electronic structure of the fully polarized state of EuAgAs (see the SM) [40]. We find that each Dirac node indeed splits into a pair of Weyl nodes of opposite chiral charge, realizing a ferromagnetic Weyl semimetal. The distance between two pairs of Weyl nodes is $k_{w1} = 0.1096$ Å^{-1} and $k_{w2} = 0.227$ Å^{-1}. The calculated anomalous Hall conductivity using the expression $|\sigma^A_{yx}| = [(k_{w1} + k_{w2})/2\pi] \times (e^2/h)$ [75–78] is found to be 208 $\Omega^{-1}\,\mathrm{cm}^{-1}$, which is lower than our experimentally observed maximum amplitude of $\sim$2700 $\Omega^{-1}\,\mathrm{cm}^{-1}$ at 2 K. The fact that EuAgAs belongs to a symmetry group which supports real-space Berry curvature associated with a nontrivial spin texture similar to MnNiGa and MnPdGa [25,26] makes the THE a natural choice for the additional contribution.

In summary, using first-principles calculations, we show that EuAgAs hosts an antiferromagnetic DSM ground state with a pair of Dirac cones. The observed magnetic properties confirm that EuAgAs shows an AFM transition at $T_N = 12$ K along with a weak metamagnetic transition below T_N. Chiral anomaly induced positive longitudinal MC confirms the presence of a Weyl fermion state in EuAgAs under an applied magnetic field. It further exhibits anomalous and topological Hall effects. We provide compelling evidence of the topological Hall effect in a spin-only divalent europium compound that is likely to inspire further studies on the topological Hall effect in DSMs.

Research support from IIT Kanpur is gratefully acknowledged. Z.H. also acknowledges support from SERB India (Grant No. CRG/2018/000220). A.A. acknowledges the Science and Engineering Research Board (SERB) and Department of Science and Technology (DST) of the Government of India for financial support. The work at TIFR Mumbai is supported by the Department of Atomic Energy of the Government of India under Project No. 12-R&D-TFR-5.10-0100. We thank Arup Ghosh for Hall resistivity measurements.

[1] N. P. Armitage, E. J. Mele, and A. Vishwanath, Rev. Mod. Phys. **90**, 015001 (2018).
[2] B. Yan and C. Felser, Annu. Rev. Condens. Matter Phys. **8**, 337 (2017).
[3] M. Z. Hasan and C. L. Kane, Rev. Mod. Phys. **82**, 3045 (2010).
[4] X.-L. Qi and S.-C. Zhang, Rev. Mod. Phys. **83**, 1057 (2011).
[5] M. Neupane, N. Alidoust, S.-Y. Xu, T. Kondo, Y. Ishida, D. J. Kim, C. Liu, I. Belopolski, Y. J. Jo, T.-R. Chang, H.-T. Jeng, T. Durakiewicz, L. Balicas, H. Lin, A. Bansil, S. Shin, Z. Fisk, and M. Z. Hasan, Nat. Commun. **4**, 2991 (2013).
[6] A. Laha, S. Malick, R. Singha, P. Mandal, P. Rambabu, V. Kanchana, and Z. Hossain, Phys. Rev. B **99**, 241102(R) (2019).
[7] A. Laha, S. Mardanya, B. Singh, H. Lin, A. Bansil, A. Agarwal, and Z. Hossain, Phys. Rev. B **102**, 035164 (2020).
[8] A. Laha, P. Rambabu, V. Kanchana, L. Petit, Z. Szotek, and Z. Hossain, Phys. Rev. B **102**, 235135 (2020).
[9] N. Morali, R. Batabyal, P. K. Nag, E. Liu, Q. Xu, Y. Sun, B. Yan, C. Felser, N. Avraham, and H. Beidenkopf, Science **365**, 1286 (2019).
[10] I. Belopolski, K. Manna, D. S. Sanchez, G. Chang, B. Ernst, J. Yin, S. S. Zhang, T. Cochran, N. Shumiya, H. Zheng, B. Singh, G. Bian, D. Multer, M. Litskevich, X. Zhou, S.-M. Huang, B. Wang, T.-R. Chang, S.-Y. Xu, A. Bansil *et al.*, Science **365**, 1278 (2019).
[11] E. Liu, Y. Sun, N. Kumar, L. Muechler, A. Sun, L. Jiao, S.-Y. Yang, D. Liu, A. Liang, Q. Xu, J. Kroder, V. Süß, H. Borrmann, C. Shekhar, Z. Wang, C. Xi, W. Wang, W. Schnelle, S. Wirth, Y. Chen *et al.*, Nat. Phys. **14**, 1125 (2018).
[12] Q. Wang, Y. Xu, R. Lou, Z. Liu, M. Li, Y. Huang, D. Shen, H. Weng, S. Wang, and H. Lei, Nat. Commun. **9**, 3681 (2018).
[13] Y. Zhu, B. Singh, Y. Wang, C.-Y. Huang, W.-C. Chiu, B. Wang, D. Graf, Y. Zhang, H. Lin, J. Sun, A. Bansil, and Z. Mao, Phys. Rev. B **101**, 161105(R) (2020).
[14] A. Mook, J. Henk, and I. Mertig, Phys. Rev. Lett. **117**, 157204 (2016).
[15] K. Li, C. Li, J. Hu, Y. Li, and C. Fang, Phys. Rev. Lett. **119**, 247202 (2017).
[16] F.-Y. Li, Y.-D. Li, Y. B. Kim, L. Balents, Y. Yu, and G. Chen, Nat. Commun. **7**, 12691 (2016).
[17] W. Yao, C. Li, L. Wang, S. Xue, Y. Dan, K. Iida, K. Kamazawa, K. Li, C. Fang, and Y. Li, Nat. Phys. **14**, 1011 (2018).
[18] T. Liang, J. Lin, Q. Gibson, S. Kushwaha, M. Liu, W. Wang, H. Xiong, J. A. Sobota, M. Hashimoto, P. S. Kirchmann, Z.-X. Shen, R. J. Cava, and N. P. Ong, Nat. Phys. **14**, 451 (2018).
[19] T. Suzuki, R. Chisnell, A. Devarakonda, Y.-T. Liu, W. Feng, D. Xiao, J. W. Lynn, and J. G. Checkelsky, Nat. Phys. **12**, 1119 (2016).
[20] P. Bruno, V. K. Dugaev, and M. Taillefumier, Phys. Rev. Lett. **93**, 096806 (2004).
[21] W. Wang, M. W. Daniels, Z. Liao, Y. Zhao, J. Wang, G. Koster, G. Rijnders, C.-Z. Chang, D. Xiao, and W. Wu, Nat. Mater. **18**, 1054 (2019).
[22] A. Neubauer, C. Pfleiderer, B. Binz, A. Rosch, R. Ritz, P. G. Niklowitz, and P. Böni, Phys. Rev. Lett. **102**, 186602 (2009).
[23] N. Kanazawa, Y. Onose, T. Arima, D. Okuyama, K. Ohoyama, S. Wakimoto, K. Kakurai, S. Ishiwata, and Y. Tokura, Phys. Rev. Lett. **106**, 156603 (2011).
[24] T. Schulz, R. Ritz, A. Bauer, M. Halder, M. Wagner, C. Franz, C. Pfleiderer, K. Everschor, M. Garst, and A. Rosch, Nat. Phys. **8**, 301 (2012).
[25] W. Wang, Y. Zhang, G. Xu, L. Peng, B. Ding, Y. Wang, Z. Hou, X. Zhang, X. Li, E. Liu, S. Wang, J. Cai, F. Wang, J. Li,

F. Hu, G. Wu, B. Shen, and X.-X. Zhang, Adv. Mater. **28**, 6887 (2016).
[26] X. Xiao, L. Peng, X. Zhao, Y. Zhang, Y. Dai, J. Guo, M. Tong, J. Li, B. Li, W. Liu, J. Cai, B. Shen, and Z. Zhang, Appl. Phys. Lett. **114**, 142404 (2019).
[27] P. Puphal, V. Pomjakushin, N. Kanazawa, V. Ukleev, D. J. Gawryluk, J. Ma, M. Naamneh, N. C. Plumb, L. Keller, R. Cubitt, E. Pomjakushina, and J. S. White, Phys. Rev. Lett. **124**, 017202 (2020).
[28] T. Kurumaji, T. Nakajima, V. Ukleev, A. Feoktystov, T.-h. Arima, K. Kakurai, and Y. Tokura, Phys. Rev. Lett. **119**, 237201 (2017).
[29] I. Kézsmárki, S. Bordács, P. Milde, E. Neuber, L. M. Eng, J. S. White, H. M. Rønnow, C. D. Dewhurst, M. Mochizuki, K. Yanai, H. Nakamura, D. Ehlers, V. Tsurkan, and A. Loidl, Nat. Mater. **14**, 1116 (2015).
[30] C. Sürgers, G. Fischer, P. Winkel, and H. v. Löhneysen, Nat. Commun. **5**, 3400 (2014).
[31] B. G. Ueland, C. F. Miclea, Y. Kato, O. Ayala-Valenzuela, R. D. McDonald, R. Okazaki, P. H. Tobash, M. A. Torrez, F. Ronning, R. Movshovich, Z. Fisk, E. D. Bauer, I. Martin, and J. D. Thompson, Nat. Commun. **3**, 1067 (2012).
[32] Y. Taguchi, Y. Oohara, H. Yoshizawa, N. Nagaosa, and Y. Tokura, Science **291**, 2573 (2001).
[33] Y. Machida, S. Nakatsuji, Y. Maeno, T. Tayama, T. Sakakibara, and S. Onoda, Phys. Rev. Lett. **98**, 057203 (2007).
[34] Y. Ohuchi, Y. Kozuka, M. Uchida, K. Ueno, A. Tsukazaki, and M. Kawasaki, Phys. Rev. B **91**, 245115 (2015).
[35] L. Vistoli, W. Wang, A. Sander, Q. Zhu, B. Casals, R. Cichelero, A. Barthélémy, S. Fusil, G. Herranz, S. Valencia, R. Abrudan, E. Weschke, K. Nakazawa, H. Kohno, J. Santamaria, W. Wu, V. Garcia, and M. Bibes, Nat. Phys. **15**, 67 (2019).
[36] S. X. Huang and C. L. Chien, Phys. Rev. Lett. **108**, 267201 (2012).
[37] T. Taniguchi, K. Yamanaka, H. Sumioka, T. Yamazaki, Y. Tabata, and S. Kawarazaki, Phys. Rev. Lett. **93**, 246605 (2004).
[38] F. W. Fabris, P. Pureur, J. Schaf, V. N. Vieira, and I. A. Campbell, Phys. Rev. B **74**, 214201 (2006).
[39] J. Nayak, N. Kumar, S.-C. Wu, C. Shekhar, J. Fink, E. D. L. Rienks, G. H. Fecher, Y. Sun, and C. Felser, J. Phys.: Condens. Matter **30**, 045501 (2018).
[40] See Supplemental Material at http://link.aps.org/supplemental/10.1103/PhysRevB.103.L241112 for details of the synthesis, computations, band structure, and magnetic and transport measurements.
[41] J. Rodríguez-Carvajal, Phys. B (Amsterdam) **192**, 55 (1993).
[42] P. Hohenberg and W. Kohn, Phys. Rev. **136**, B864 (1964).
[43] W. Kohn and L. J. Sham, Phys. Rev. **140**, A1133 (1965).
[44] P. E. Blöchl, Phys. Rev. B **50**, 17953 (1994).
[45] G. Kresse and J. Furthmüller, Phys. Rev. B **54**, 11169 (1996).
[46] G. Kresse and D. Joubert, Phys. Rev. B **59**, 1758 (1999).
[47] J. P. Perdew, K. Burke, and M. Ernzerhof, Phys. Rev. Lett. **77**, 3865 (1996).
[48] V. Anisimov, A. Poteryaev, M. Korotin, A. Anokhin, and G. Kotliar, J. Phys.: Condens. Matter **9**, 7359 (1997).
[49] V. I. Anisimov, J. Zaanen, and O. K. Andersen, Phys. Rev. B **44**, 943 (1991).
[50] A. Laha and Z. Hossain, J. Magn. Magn. Mater. **465**, 654 (2018).
[51] B. K. Cho, P. C. Canfield, and D. C. Johnston, Phys. Rev. B **53**, 8499 (1996).
[52] J. Tong, J. Parry, Q. Tao, G.-H. Cao, Z.-A. Xu, and H. Zeng, J. Alloys Compd. **602**, 26 (2014).
[53] C. Feng, Z. Ren, S. Xu, S. Jiang, Z. Xu, G. Cao, I. Nowik, I. Felner, K. Matsubayashi, and Y. Uwatoko, Phys. Rev. B **82**, 094426 (2010).
[54] U. B. Paramanik, R. Prasad, C. Geibel, and Z. Hossain, Phys. Rev. B **89**, 144423 (2014).
[55] J. Y. Chan, S. M. Kauzlarich, P. Klavins, R. N. Shelton, and D. J. Webb, Phys. Rev. B **57**, R8103(R) (1998).
[56] S. Majumdar, R. Mallik, E. V. Sampathkumaran, K. Rupprecht, and G. Wortmann, Phys. Rev. B **60**, 6770 (1999).
[57] J. Hu, T. F. Rosenbaum, and J. B. Betts, Phys. Rev. Lett. **95**, 186603 (2005).
[58] H.-J. Kim, K.-S. Kim, J.-F. Wang, M. Sasaki, N. Satoh, A. Ohnishi, M. Kitaura, M. Yang, and L. Li, Phys. Rev. Lett. **111**, 246603 (2013).
[59] K. Das and A. Agarwal, Phys. Rev. Research **2**, 013088 (2020).
[60] S. Nishihaya, M. Uchida, Y. Nakazawa, K. Akiba, M. Kriener, Y. Kozuka, A. Miyake, Y. Taguchi, M. Tokunaga, and M. Kawasaki, Phys. Rev. B **97**, 245103 (2018).
[61] H. Ishizuka and M. Sato, Phys. Rev. B **100**, 224411 (2019).
[62] C. Y. Guo, F. Wu, Z. Z. Wu, M. Smidman, C. Cao, A. Bostwick, C. Jozwiak, E. Rotenberg, Y. Liu, F. Steglich, and H. Q. Yuan, Nat. Commun. **9**, 4622 (2018).
[63] A. A. Abrikosov, Europhys. Lett. **49**, 789 (2000).
[64] Q. Li, D. E. Kharzeev, C. Zhang, Y. Huang, I. Pletikosić, A. V. Fedorov, R. D. Zhong, J. A. Schneeloch, G. D. Gu, and T. Valla, Nat. Phys. **12**, 550 (2016).
[65] M. M. Jadidi, M. Kargarian, M. Mittendorff, Y. Aytac, B. Shen, J. C. König-Otto, S. Winnerl, N. Ni, A. L. Gaeta, T. E. Murphy, and H. D. Drew, Phys. Rev. B **102**, 245123 (2020).
[66] C.-L. Zhang, S.-Y. Xu, I. Belopolski, Z. Yuan, Z. Lin, B. Tong, G. Bian, N. Alidoust, C.-C. Lee, S.-M. Huang, T.-R. Chang, G. Chang, C.-H. Hsu, H.-T. Jeng, M. Neupane, D. S. Sanchez, H. Zheng, J. Wang, H. Lin, C. Zhang *et al.*, Nat. Commun. **7**, 10735 (2016).
[67] K. Shrestha, M. Chou, D. Graf, H. D. Yang, B. Lorenz, and C. W. Chu, Phys. Rev. B **95**, 195113 (2017).
[68] G. Xu, W. Wang, X. Zhang, Y. Du, E. Liu, S. Wang, G. Wu, Z. Liu, and X. X. Zhang, Sci. Rep. **4**, 5709 (2014).
[69] Z. Hou, Y. Wang, G. Xu, X. Zhang, E. Liu, W. Wang, Z. Liu, X. Xi, W. Wang, and G. Wu, Appl. Phys. Lett. **106**, 102102 (2015).
[70] H. Li, H. He, H.-Z. Lu, H. Zhang, H. Liu, R. Ma, Z. Fan, S.-Q. Shen, and J. Wang, Nat. Commun. **7**, 10301 (2016).
[71] Y. Li, N. Kanazawa, X. Z. Yu, A. Tsukazaki, M. Kawasaki, M. Ichikawa, X. F. Jin, F. Kagawa, and Y. Tokura, Phys. Rev. Lett. **110**, 117202 (2013).
[72] S. Nakatsuji, N. Kiyohara, and T. Higo, Nature (London) **527**, 212 (2015).
[73] A. K. Nayak, J. E. Fischer, Y. Sun, B. Yan, J. Karel, A. C. Komarek, C. Shekhar, N. Kumar, W. Schnelle, J. Kübler, C. Felser, and S. S. P. Parkin, Sci. Adv. **2**, e1501870 (2016).
[74] R. Singha, S. Roy, A. Pariari, B. Satpati, and P. Mandal, Phys. Rev. B **99**, 035110 (2019).

[75] A. A. Burkov and L. Balents, Phys. Rev. Lett. **107**, 127205 (2011).

[76] M. Uchida, T. Koretsune, S. Sato, M. Kriener, Y. Nakazawa, S. Nishihaya, Y. Taguchi, R. Arita, and M. Kawasaki, Phys. Rev. B **100**, 245148 (2019).

[77] L. Šmejkal, Y. Mokrousov, B. Yan, and A. H. MacDonald, Nat. Phys. **14**, 242 (2018).

[78] M. Hirschberger, S. Kushwaha, Z. Wang, Q. Gibson, S. Liang, C. Belvin, B. A. Bernevig, R. J. Cava, and N. P. Ong, Nat. Mater. **15**, 1161 (2016).